

# Structural and Functional Properties of the Thin-Film System Ti-Ni-Si

M. Wambach, P. Ziolkowski, E. Müller, A. Ludwig

## Abstract

The thin-film system Ti-Ni-Si was investigated using combinatorial materials science methods. A thin-film composition spread library of the system was fabricated using combinatorial magnetron sputtering. The functional properties Seebeck coefficient, electrical resistivity and luminance were determined using high-throughput characterization techniques. A thin-film phase diagram was established by the assessment of high-throughput X-ray diffraction results. Correlations between composition, phase constitution and functional properties with focus on the binary composition space are discussed.

## Introduction

The Ti-Ni-Si system contains a high number of phases with interesting properties. Ti- and Ni-silicides are of interest as contacts and gate electrodes in transistors [1, 2, 3, 4, 5, 6] due to their low electrical resistivity (e.g. 24, 14 and 34  $\mu\Omega\text{m}$  for  $\text{Ni}_2\text{Si}$ ,  $\text{NiSi}$  and  $\text{NiSi}_2$ , respectively [3]) and integratibility into CMOS processing.  $\text{Ti}_5\text{Si}_3$  is a potential high-temperature structural material due to its high melting point of 2403 K [7]. This applies similarly to  $\text{Ni}_3\text{Ti}$  and  $\text{Ni}_3\text{Si}$  [8, 9].  $\text{NiSi}$  and  $\text{NiSi}_2$  have been investigated as a Li-battery electrode material [10, 11, 12].  $\text{Ti}_4\text{Ni}_4\text{Si}_7$  was also investigated as an anode material for Li-ion batteries [13]. Chang et al. found excellent field emission properties in  $\text{Ti}_5\text{Si}_4$  nanobats [14].  $\text{NiTi}$  is a known shape memory alloy (SMA) [15, 16, 17]. The  $\text{Ti}_6\text{Ni}_{16}\text{Si}_7$  phase, also called G-phase, is a known precipitate in steels and was investigated as a candidate for superconductivity [18, 19].  $\text{Ti}_2\text{Ni}$  has been tested as a hydrogen

storage material [20] as well as for its high-temperature wear properties [21]. Wear and corrosion properties of material systems including  $\text{Ti}_2\text{Ni}_3\text{Si}$  and  $\text{NiTi}$  were found to be favorable, making this system a viable choice as a coating material for harsh environment applications [22]. No experimental data on functional properties has been published for the phases  $\text{TiNi}_4\text{Si}_3$  and  $\text{TiNiSi}$ . Materials within the ternary Ti-Ni-Si compositional space have also been investigated for their functional properties including the glass forming ability [23], the use as shape-memory alloys [24,25,26,27] or as a bonding material for carbon composites [28]. In a study on the glass forming ability within the Ti-Ni-Sn system, the compositional space of  $52.5 \text{ at.}\% \leq \text{Ti} \leq 67.5 \text{ at.}\%$ ,  $27.5 \text{ at.}\% \leq \text{Ni} \leq 45 \text{ at.}\%$  and  $2.5 \text{ at.}\% \leq \text{Si} \leq 17.5 \text{ at.}\%$  was chosen. Out of this compositional space the composition  $\text{Ti}_{57}\text{Ni}_{35}\text{Si}_8$  was identified as the best glass former [23]. Kim investigated ribbons with a composition of  $\text{Ti}_{50}\text{Ni}_{49}\text{Si}_1$  and  $\text{Ti}_{50}\text{Ni}_{47}\text{Si}_3$  for their martensitic transformation behavior [24]. Arc melted samples with a composition range of  $\text{Ti}_{51}\text{Ni}_{49-x}\text{Si}_x$  ( $x = 0, 1$  and  $2$ ) were investigated by Ibrahim et al. [25] while Hsieh et al. investigated the compositions  $\text{Ti}_{50-x}\text{Ni}_{50}\text{Si}_x$ ,  $\text{Ti}_{50}\text{Ni}_{50-x}\text{Si}_x$  and  $\text{Ti}_{51}\text{Ni}_{49-x}\text{Si}_x$  ( $x = 1$  and  $2$ ) [26]. Kim et al. investigated alloys fabricated by vacuum induction melting with a composition of  $\text{Ti}_{50}\text{Ni}_{50-x}\text{Si}_x$  ( $x = 2, 4, 6$ ) and  $\text{Ti}_{50-x}\text{Ni}_{50}\text{Si}_x$  ( $x = 2, 5, 7, 10$ ) for their shape memory properties [27]. Wang et al. investigated  $\text{Ti}_{17}\text{Ni}_{17}\text{Si}_{66}$  as an interlayer to bond carbon composites [28].

Modern engineering materials are characterized by increasing chemical complexity and functional requirements and it becomes more and more challenging to comprehensively correlate structure-property relationships in these materials, using a classical sample-by-sample approach [29]. Combinatorial materials science methods are efficient means to explore such complex materials systems. This is due to the ability to fabricate material libraries, e.g. complete ternary systems [30], in a single fabrication step and characterize their properties in a high-throughput manner.

Ternary phase diagrams of the system Ti-Ni-Si at 750°C / 800°C [31,32] and 1100°C [33] can be found in the ASM Alloy Phase Diagram Database. Tokunaga et al. published a thermodynamic analysis of the Ti-Ni-Si system comparing their theoretical results to the afore mentioned ternary phase diagrams among others [34]. Weitzer et al. published a revised version of their earlier publication of the Ti-Ni-Si system at 900 °C [35]. While all ternary diagrams include the ternary phases  $\text{Ti}_2\text{Ni}_3\text{Si}$  (G' phase),  $\text{Ti}_4\text{Ni}_4\text{Si}_7$  (V phase),  $\text{Ti}_6\text{Ni}_{16}\text{Si}_7$  (G phase, also:  $\text{Ti}_6\text{Ni}_{16}\text{Si}_8$  and  $\text{Ti}_6\text{Ni}_{17}\text{Si}_7$ ),  $\text{TiNi}_4\text{Si}_3$  (G'' phase) and  $\text{TiNiSi}$  (E phase), some publication claim the existence of the  $\text{Ti}_4\text{NiSi}_4$  (H phase) [33],  $\text{Ni}_5\text{SiTi}_6$  (X phase) or  $\tau_6$  ( $\text{Ti}_{53}\text{Ni}_6\text{Si}_{41}$ ) and  $\tau_7$  ( $\text{Ti}_{42}\text{Ni}_{16}\text{Si}_{42}$ ) [35] phases. On the binary Ni-Ti axis the three phases  $\text{Ni}_3\text{Ti}$ ,  $\text{NiTi}$  and  $\text{NiTi}_2$  are detected by all publication except for the phase diagram by Hu et al. where the compositional region around  $\text{NiTi}_2$  is liquid at 1100°C [33]. On the Ti-Si axis, all published phase diagrams include the  $\text{TiSi}_2$ ,  $\text{TiSi}$  and  $\text{Ti}_5\text{Si}_3$  phase. The  $\text{Ti}_5\text{Si}_4$  and  $\text{Ti}_3\text{Si}$  phases were not identified by Markiv et al. [31,32], the latter was also not detected by Hu et al. On the binary Ni-Si axis the identified phases highly depend on the temperature. At 800°C and below the phases  $\text{NiSi}_2$ ,  $\text{NiSi}$ ,  $\text{Ni}_3\text{Si}_2$ ,  $\text{Ni}_2\text{Si}$ ,  $\text{Ni}_{31}\text{Si}_{12}$  and  $\text{Ni}_3\text{Si}$  have been identified by Markiv et al., while, at higher temperatures, the high temperature modification of  $\text{Ni}_2\text{Si}$  and  $\text{Ni}_3\text{Si}$  as well as the phase  $\text{Ni}_5\text{Si}_2$  are identified. At 1100°C Hu et al. identified the region around  $\text{NiSi}$  as a liquid, while the  $\text{NiSi}_2$  phase is not identified.

Here, the thin-film Ti-Ni-Si system is investigated for its electrical resistivity, luminance and Seebeck coefficient. With rising interest in silicide-based thermoelectric materials due to the abundance of their constituents and intoxicity [36,37], silicides within the Ti-Ni-Si system are worth to be investigated for their resistivity and Seebeck coefficient values. It has been demonstrated that the luminance of materials can be used to distinguish between phases or phase fields [38].

## Experimental Methods

Thin-film composition spread-type materials libraries (ML) of the Ti-Ni-Si system were fabricated on patterned 100 mm diameter polycrystalline aluminum oxide ( $\text{Al}_2\text{O}_3$ , Kyocera Corporation,  $R_a = 20$  nm) wafers using a combinatorial magnetron sputtering system (DCA Instruments Oy). The pattern consists of small numbered crosses produced by lithography. After the deposition of the film, the photo resist is stripped in an ultrasonic bath leaving the crosses and numbers bare of the sputtered film. The structures are used to create a defined step as well as to geometrically define each of the 342 measurement areas.  $\text{Al}_2\text{O}_3$  wafers, instead of  $\text{SiO}_2$  wafers, were chosen to enable the measurement of the Si content in the ML using EDX, to achieve a good film adhesion to the substrate and to assure inertness of the oxide during annealing. The used sputter system is a six-cathode arrangement where all cathodes are mounted on a single rail. A sputtered multilayered precursor thin-film library comprising of different thin-film wedges from elemental sources is fabricated by sequentially and periodically sputtering from the cathodes. Shutters are used to create continuous thickness gradients across the substrate. By rotating the substrate by  $120^\circ$  for each element a complete coverage of the ternary composition space can be achieved. This technique results in wedge-type multilayered thin films [39]. Here, 120 individual wedges with a mean thickness of 4 nm in the center of the ML were deposited, resulting in a mean film thickness of 480 nm.

The ML was sputtered from elemental targets with a diameter of 101.6 mm (4 inches). The used sputter targets had a thickness of 3.175 mm (Si), 3 mm (Ni) and 6.35 mm (Ti). The purity values of the targets were 99.99 at.% for Ti (Goodfellow Cambridge Limited), 99.999 at.% for Si (AJA International Incorporated) and 99.995 at.% for Ni (Kurt J. Lesker Company). To reduce thermal shock, the Si target was bonded to a Cu plate. Before deposition, the sputter chamber was

evacuated to a pressure of  $1 \cdot 10^{-5}$  Pa. During the deposition, a pressure of 0.67 Pa was maintained with an Ar flow of  $1 \cdot 10^{-6} \text{ m}^3 \text{ s}^{-1}$ . The ML was annealed ex-situ at 1073 K for one hour in vacuum ( $1.3 \cdot 10^{-7}$ - $1.3 \cdot 10^{-6}$  Pa). The composition of each measurement area on the ML was mapped using a SEM (Joel 5800) equipped with an EDX detector (Inca X-act, Oxford Instruments). The electrical resistance of the thin films was measured using an in-house built 4-point high-throughput resistance measurement system [40]. To measure the film thickness on photolithographically created steps a tactile profilometer (XP2, Ambios Technology) was used. The electrical resistivity was calculated from resistance and thickness data. The diffraction patterns of the ML were measured using an X-ray diffractometer (XRD, PANalytical X'Pert Pro, wavelength: 0.154 nm [Cu K $\alpha$ ]). The ML was mapped in a  $\theta/2$ - $\theta$ -scan in Bragg-Brentano geometry in a range from 27° to 100°. Pictures of the ML were taken using an in-house built photo setup [41].

The measurement of the spatial Seebeck coefficient distribution on the ML was accomplished by means of the Potential & Seebeck Microprobe (PSM)[42]. The PSM apparatus is composed of an in-house built heated copper probe tip, an xyz positioning stage (x.Act LT Series, Linos), two type T thermocouples (XF-322-FAR, Labfacility), and a digital multimeter for data acquisition (Model 2700, Keithley). One thermocouple is mounted at the copper probe which contains a tungsten carbide tip at its apex with a contact diameter of 12  $\mu\text{m}$ . The other thermocouple is fixed to the top surface of the ML with Ag paste. In order to ensure isothermal conditions within the sample during the lift-off phase of the scanning tip the ML is mounted on a passive heat sink. During touch down of the heated probe tip onto the ML a microscopic volume of the thin film is heated in the vicinity of the contact area, causing a thermal gradient to spread across the film. Thermovoltages are generated by the ML in response to this gradient on the length scale of the

expansion of the thermal field within the film. The uncertainty of the obtained Seebeck value is associated with inherent methodical error sources [42] and ranges typically from 6% to 25% for thin-film samples made from degenerate semiconductors. For homogeneous areas of the thin film (relatively to the heated ML volume) the accuracy of Seebeck coefficient measurements is related to the thermal resistances of the ML and the substrate material being used. Both properties scale with the thickness and inversely proportional to the thermal conductivity. According to a previous study [<sup>43</sup>] on a thermoelectric TiNiSn ML with a thickness of 400 nm deposited on an Al<sub>2</sub>O<sub>3</sub> substrate the deviation of the measured Seebeck coefficient can reach 25% and more. The Seebeck coefficient measured on inhomogeneities with a lateral dimension of at least 300  $\mu$ m can be resolved for this combination of sample thickness and substrate material with a maximum deviation of 10% compared to the homogeneous case. These values have been determined for a comparable thickness and same substrate material as used in this study. However, the capability to reveal relative variations of the Seebeck coefficients for different phases on a ML is related to the spatial resolution of the instrument. The spatial resolution is related to the distribution of the thermal and electrical conductivities within the sample, which determine the significance of eddy currents due to their impact on the measured thermovoltages [43,44]. These currents are induced by the different thermovoltages being generated in response to a thermal gradient, which spreads over the transition between different phases having different Seebeck coefficient. The significance of the spurious effect on the Seebeck measurement by eddy currents is linked to their Ohmic voltage drop across the different phases, which overlays the generated thermovoltages in a two-phase region exposed to a temperature gradient. Once metallic phases are involved, only minor voltage drops can be expected due to high electrical conductivity and relatively low thermovoltages generated by the typically low Seebeck coefficients of metallic phases, i.e. a metallic inclusion will short-circuit the thermo-voltage of a neighboring semiconducting phase.

Differences of the Seebeck coefficient of adjacent metallic phases can be revealed with a similar relative error of 1-2% [42] as it is expected for the mapping of transitions between semiconducting phases. Consequently, the setup is considered to allow mappings on MLs in a high-throughput manner with sufficient high sensitivity.

## Results and Discussion

Figure 1 shows the compositional distribution of Ti, Ni and Si in the ML. Figures 1a) to 1c) show the compositional gradients of the individual elements as well as the angular arrangement of  $120^\circ$  between the gradients. The curvature of the elemental spreads perpendicular to the gradient is due

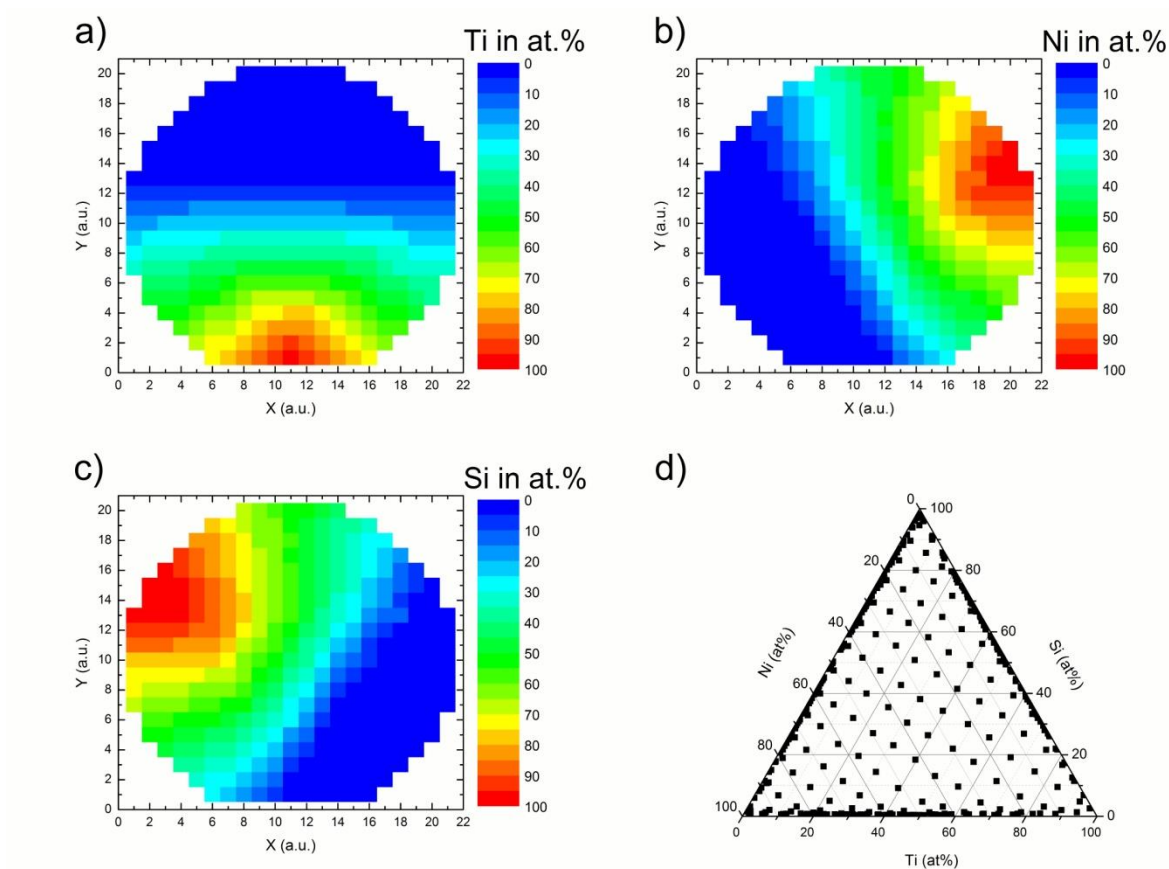


Figure 1: a) - c) Color-coded visualization of the Ti-, Ni-, and Si-content of the materials library, d) complete compositional coverage of the Ti-Ni-Si materials library in the ternary diagram.

to the difference in deposition rate from the center to the edge of the sputtering target. Figure 1d)

shows all compositions determined by EDX in 342 measurement areas in a ternary composition diagram illustrating that the full system was covered.

Figure 2 shows a sketch of the ternary phase diagram based on the XRD measurement of the Ti-Ni-Si thin-film materials library fabricated in this study. The ternary phases  $\text{Ti}_2\text{Ni}_3\text{Si}$  (G' phase, hexagonal,  $\text{P6}_3/\text{mmc}$ ),  $\text{Ti}_4\text{Ni}_4\text{Si}_7$  (V phase, tetragonal,  $\text{I4}/\text{mmm}$ ),  $\text{Ti}_6\text{Ni}_{16}\text{Si}_7$  (G phase, cubic,  $\text{Fm-3m}$ , also:  $\text{Ti}_6\text{Ni}_{16}\text{Si}_8$  and  $\text{Ti}_6\text{Ni}_{17}\text{Si}_7$ ),  $\text{TiNi}_4\text{Si}_3$  (G'' phase, hexagonal,  $\text{P6}/\text{mmm}$ ),  $\text{TiNiSi}$  (E phase, orthorhombic,  $\text{Pnma}$ ) and  $\text{Ti}_4\text{NiSi}_4$  (H phase, orthorhombic,  $\text{Pnma}$ ) could be detected in the ML, while the  $\text{Ti}_6\text{Ni}_5\text{Si}$  phase (F or X phase) [45] as well as the so-called  $\tau_6$  and  $\tau_7$  phases [3534] were not observed. The binary phases  $\text{Ti}_2\text{Ni}$  (cubic,  $\text{Fd-3m}$ ),  $\text{TiNi}$  (cubic,  $\text{Pm-3m}$  / monoclinic,  $\text{P2}_1/\text{m}$ ),  $\text{TiNi}_3$  (hexagonal,  $\text{P6}_3/\text{mmc}$ ),  $\text{TiSi}_2$  (orthorhombic,  $\text{Fddd}$ ),  $\text{TiSi}$  (orthorhombic,  $\text{Pnma}$ ),  $\text{Ti}_5\text{Si}_4$

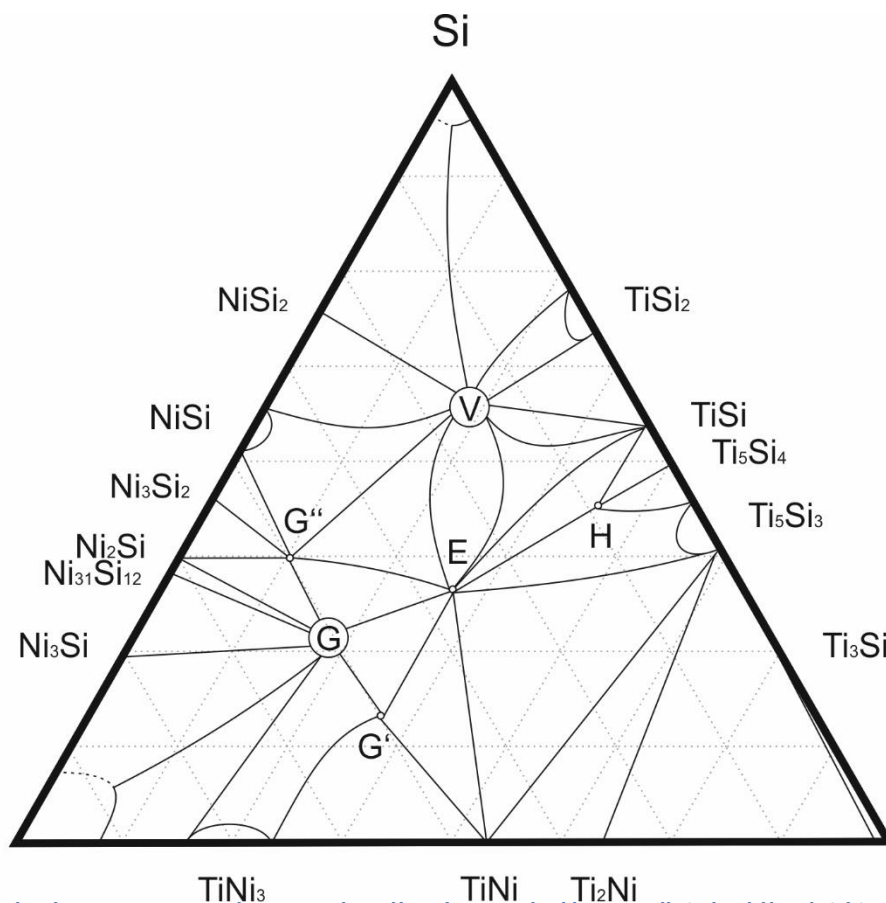


Figure 2: Scher Only the V phase do not appear as single-phase measurement areas and are therefore marked by a small circle at the stoichiometric composition. The dashed lines near pure Ni and Si indicate that the exact phase boundary between pure phases and the neighboring binary phase cannot be determined due to the neighboring phases sharing all detectable XRD peaks.



(tetragonal, P41212),  $\text{Ti}_5\text{Si}_3$  (hexagonal, P63/mcm),  $\text{Ti}_3\text{Si}$  (tetragonal, P42/n),  $\text{NiSi}_2$  (orthorhombic, Pnma),  $\text{NiSi}$  (orthorhombic, Pnma/*Pmm2*),  $\text{Ni}_3\text{Si}_2$  (orthorhombic, Cmc2<sub>1</sub>),  $\text{Ni}_2\text{Si}$  (orthorhombic, Pnma),  $\text{Ni}_{31}\text{Si}_{12}$  (hexagonal, P312) and  $\text{Ni}_3\text{Si}_x$  ( $x = 0-1$ , cubic, Pm-3m) were identified. The elemental phases are Ni (cubic, Fm-3m), Si (cubic, Fd-3m),  $\alpha$ -Ti (hexagonal, P63/mmc) and  $\beta$ -Ti (cubic, Im-3m).

The ternary phases identified in this work agree well with the work of Hu et al. [33]. The  $\tau_6$  and  $\tau_7$  phases found by Weitzer et al. were not detected, however they noted that the compositional stability range is small. The  $\text{Ti}_6\text{Ni}_5\text{Si}$  phase could not be identified. It has been disputed whether the XRD peaks belong to a NiTi phase by Hu et al.. This statement is supported by our XRD results. The binary phases found on the Ni-Si and Ti-Ni binary axis are in good agreement with the results of Markiv et al. [31,32]. Especially on the Ni-Si line binary high temperature phases form at temperatures above 800 °C. On the Ti-Si axis the results of this work are in good agreement with the results published by Weitzer et al. [35]. In agreement with their work, no XRD peaks of the  $\text{Ti}_3\text{Si}$  phase could be detected in the ternary composition space.

It is worth noting that the homogeneity range of some phase areas is shifted from the stoichiometric composition proposed in previous works. The offsets are likely to stem from differences in microstructure evolution of thin films compared to bulk samples. Compared to the previously published diagrams the homogeneity range appears to be higher in some single-phase (e.g.  $\text{TiNi}_3$ ,  $\text{TiSi}_2$ ) and two-phase areas (e.g.  $\text{Ti}_4\text{Ni}_4\text{Si}_7$ – $\text{TiNiSi}$ ,  $\text{Ti}_4\text{Ni}_4\text{Si}_7$ – $\text{TiSi}_2$ ). This might be due to substrate background impeding the identification of weak peaks in XRD measurements of thin film samples.

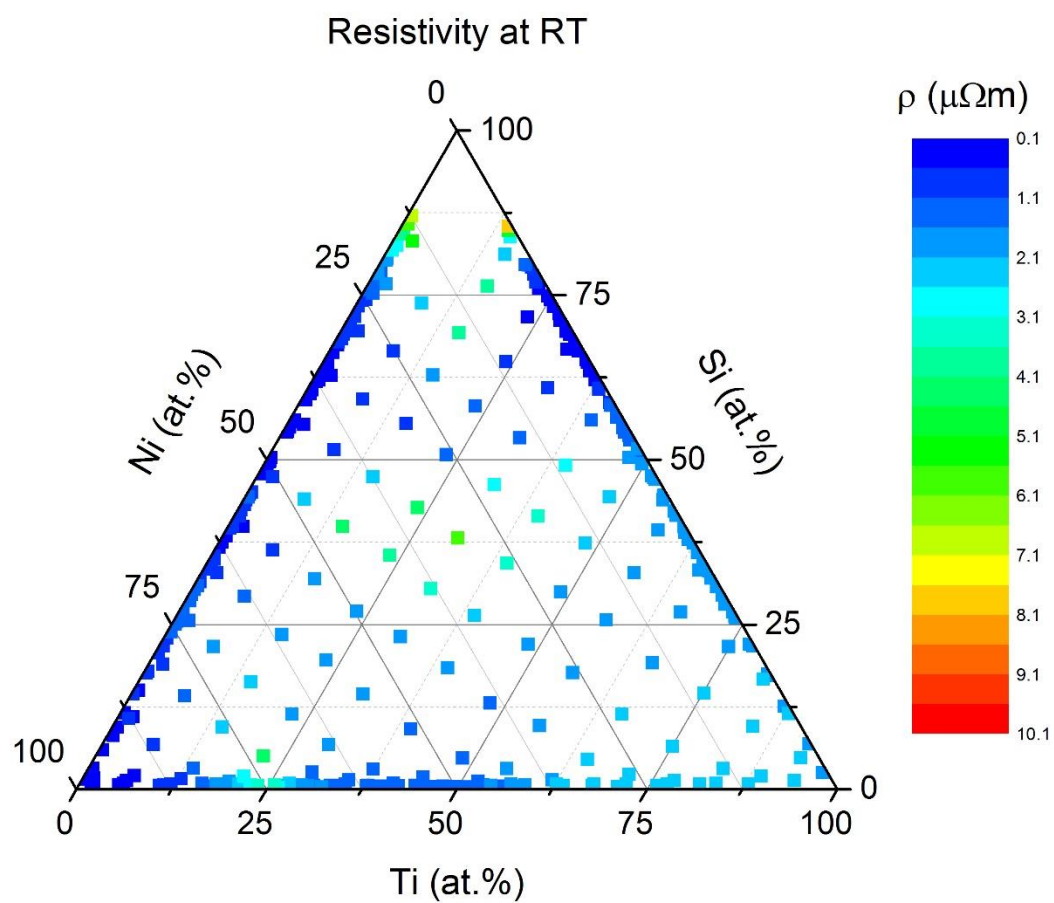


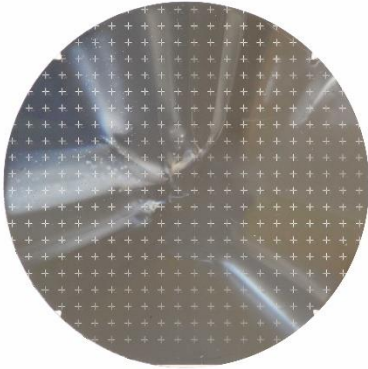
Figure 3: Color-coded plot of the resistivity at room temperature for the Ti-Ni-Si ML annealed at 1073 K for 1 h.

Figure 3 shows the resistivity plot of the annealed Ti-Ni-Si ML. Measurement areas very close to pure Si were omitted. As the electrical conductivity in this area is very low, the resistivity values for these compositions is not accessible under regular measurement conditions and are thus excluded for the analysis. Apart from the high resistivity region close to pure Si, a region with comparatively higher resistivity was identified in the center of the ternary diagram with a local maximum of  $5.7 \mu\Omega\text{m}$  for a composition of  $\text{Ti}_{31}\text{Ni}_{31}\text{Si}_{38}$ . Another region of comparatively high resistivity was identified close to the TiNi binary axis for a composition of  $\text{Ti}_{22}\text{Ni}_{73}\text{Si}_5$  ( $4.3 \mu\Omega\text{m}$ ). Regions of low resistivity were detected mainly for pure Ni, on the Ni-Si binary axis and the Ti-deficient area of the Ti-Si binary axis. Here the resistivity values are as low as  $0.2 \mu\Omega\text{m}$ .

A photo of the Ti-Ni-Si materials library (figure 4a)) shows a mixture of grey, blue-grey and yellowish areas as well as broad and thin white lines. The colors of the measurement areas were first transformed into RGB-values and then into a single luminance value. This way light and dark areas can be distinguished. Due to the fast generation of luminance data of a ML, this technique was proposed as a way to aid the identification of regions of interest on a ML [4140].

The results of the color-coded luminance are shown in figures 4b).).

a)



b)

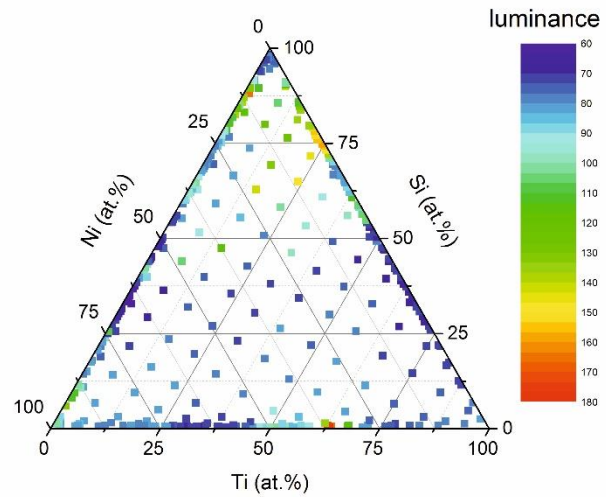


Figure 4: a) Photo of the annealed thin-film Ti-Ni-Si ML annealed at 1073 K for 1 h, b) color plot of the luminance in the ternary diagram.

Areas of high luminance were identified in the Si-rich part of the ternary diagram with values between 60 at.% and 95 at.% Si as well as on the binary Ti-Ni axis close to 60 at.% Ti and close to pure Ni. The luminance is low on the binary Ni-Si (60 at.% - 75 at.% Ni), Ti-Si (50 at.% - 85 at.% Ti) and on the Ni-Ti axis between 25 at.% and 50 at.% Ti.

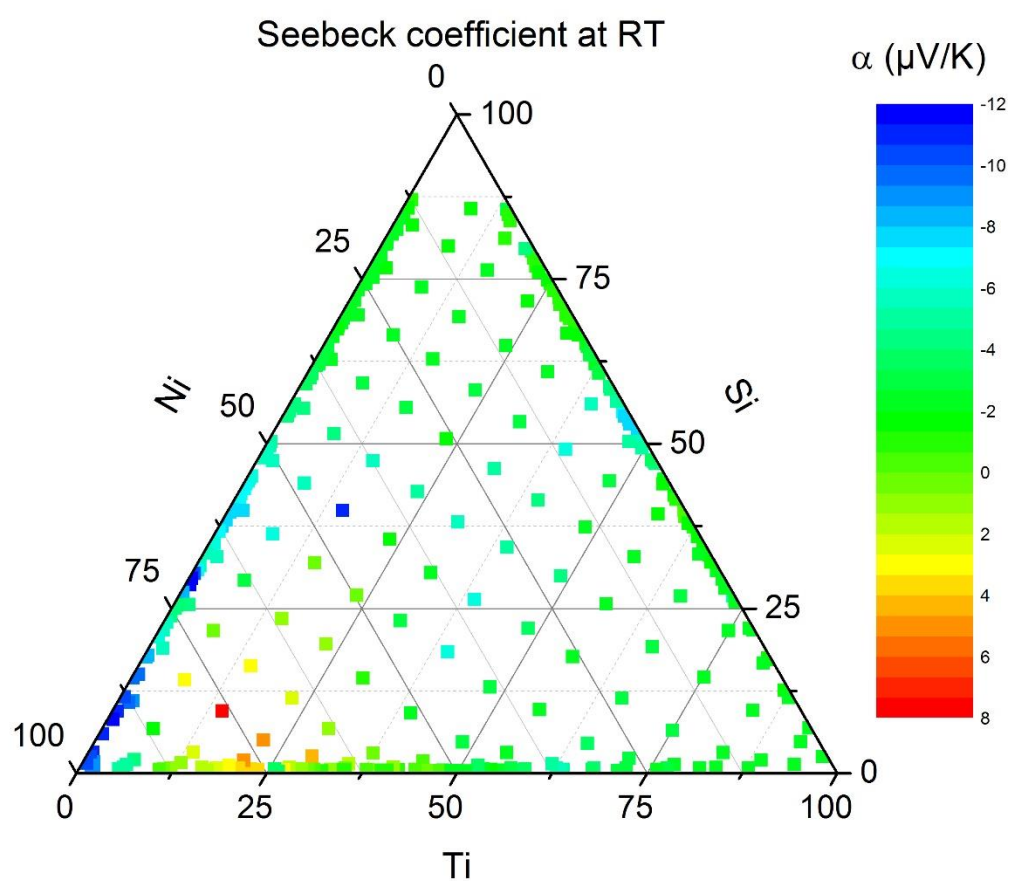


Figure 25: Color-coded visualization of the Seebeck coefficient of the thin-film Ti-Ni-Si ML annealed at 1073 K for 1 h.

Figure 5 shows the Seebeck coefficients of the thin-film Ti-Ni-Si ML. Measurement areas close to pure Si were again omitted. The PSM was designed to measure degenerate semiconductors. The high resistivity of these measurement areas increases the measurement error significantly, leading to inconsistent measurement results. Excluding the values close to pure Si, the highest p-type Seebeck coefficient is  $8 \mu\text{VK}^{-1}$  for a composition of  $\text{Ti}_{14}\text{Ni}_{76}\text{Si}_{10}$ , while the highest n-type values were measured on the Si-deficient side of the binary Ni-Si axis with a maximal amount of  $-12 \mu\text{VK}^{-1}$ . Low values were found on the binary Ti-Si axis close to 50 at.% Si. In the center of the ternary diagram, the Seebeck coefficients are preferentially n-type, showing the highest amount at  $\text{Ti}_{15}\text{Ni}_{45}\text{Si}_{40}$  ( $-11 \mu\text{VK}^{-1}$ ).

To investigate structure-function correlations in this system, the results for the binary axes, Ti-Ni, Ti-Si and Ni-Si, are discussed in detail (figure 6). In the presented library the high density of measurement areas is advantageous. The plot of the measurement areas allows for an amount of up to 1 at.% of the resulting third element.

Figure 6a) shows the resistivity, luminance and Seebeck coefficient of the Ti-Si binary axis of the measured thin film materials library. The luminance in the Si-deficient area of the plot lies between 80 for a Si content lower than 7 at.% Si and around 70 for measurement areas with a Si content between 11 at.% and 53 at.% Si. For measurement areas ranging from 53 at.% to 62 at.% Si, the luminance values are scattering between 85 and 125. In the compositional range between 62 at.% and 69 at.% Si, the values drop from 85 to 75. With increasing Si content to 75 at.% Si the luminance increases significantly from 75 to 160. With further increasing Si content the luminance values drop gradually to 70 for a Si content of 98 at.%.

The Seebeck coefficients remain fairly constant below 45 at.% Si with values in the range of  $-2.5$  to  $-1.5 \mu\text{VK}^{-1}$ . There is however a slight rise at around 39 at.% Si to  $0.5 \mu\text{VK}^{-1}$ . With increasing

Si content, the Seebeck coefficient drops to a local minimum at 53 at.% Si with a Seebeck coefficient of around  $-8 \mu\text{VK}^{-1}$ . When the Si content increases, the amount of the Seebeck coefficient decreases down to a value of around  $-1 \mu\text{VK}^{-1}$  which remains fairly constant to a composition of 85 at.% Si. With further increasing Si content, the Seebeck coefficient scatters between  $-8 \mu\text{VK}^{-1}$  and  $5.5 \mu\text{VK}^{-1}$  for values up to 96 at.% Si. For higher Si concentrations the values have been excluded.

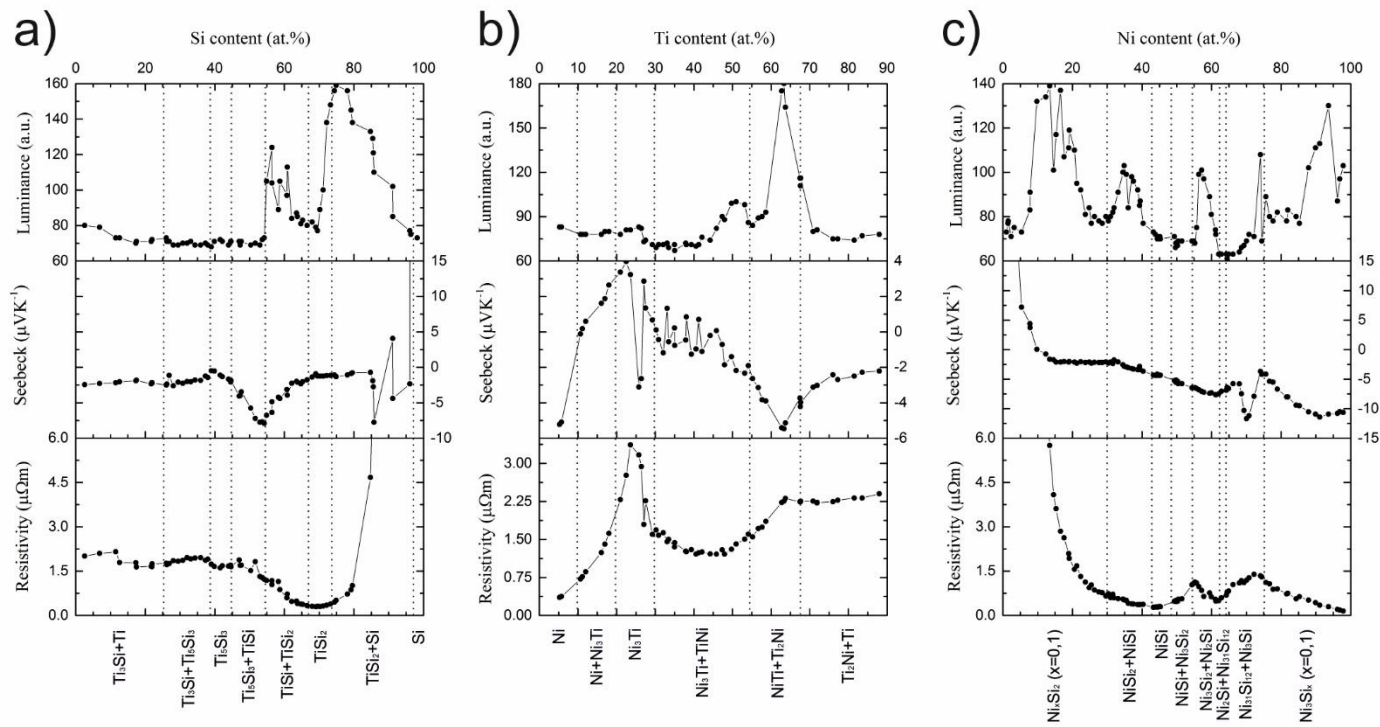


**Figure 36:** Luminance, Seebeck coefficient and electrical resistivity plotted over the Si- (a), Ti- (b) and Ni-content (c) in the Ti-Si, Ni-Ti and Ni-Si system respectively. The identified phases are shown below the plots. The dotted lines mark the borders of phase regions .



For values  $< 47$  at.% Si, the resistivity values lie in the range between  $1.5 - 2 \mu\Omega\text{m}$ . At around 12 at.% Si a slight drop in the resistivity from  $2 \mu\Omega\text{m}$  to  $1.75 \mu\Omega\text{m}$  was identified. Between a composition of  $\text{Si}_{47}\text{Ti}_{53}$  and  $\text{Si}_{69}\text{Ti}_{31}$  the resistivity is decreasing, reaching a minimum value of around  $0.3 \mu\Omega\text{m}$ . With increasing Si content, the resistivity first increases slightly, showing a rapid increase at around 80 at.% Si. For higher values the resistivity is not experimentally accessible with the applied measurement technique.

Looking at the composition  $\text{Ti}_{89}\text{Si}_{11}$ , a slight drop in the electrical resistivity and luminance can be identified. This composition also marks the onset of the formation of the  $\text{Ti}_3\text{Si}$  phase. The Seebeck coefficient however remains constant in the area. The minimum on the Seebeck coefficient at  $\text{Ti}_{47}\text{Si}_{53}$  also coincides with a significant jump in the luminance for the same composition, whereas such a significant feature cannot be assigned to the electrical resistivity. Here the TiSi phase is pronounced. At  $\text{Ti}_{31}\text{Si}_{69}$  the electrical resistivity has a local minimum. The luminance shows the onset of a significant rise at the same composition. However, the Seebeck coefficient remains fairly constant in this area. At this composition the  $\text{TiSi}_2$  phase is dominant. With increasing Si concentration pure Si forms which can be associated with the increase in resistivity and luminance.

In figure 6b) functional properties of the Ti-Ni system are plotted over the Ti content of the measurement areas. In the luminance plot, the values for low Ti contents remain fairly constant at around 80 up to 26 at.% Ti. At this composition, the luminance drops to 70. The values stay again relatively constant up to 44 at.% Ti. For increasing Ti content, the luminance values increase, showing a local maximum at around 50 at.% Ti with a luminance of 100. For a higher Ti content the luminance decreases to around 85 ( $\text{Ti}_{55}\text{Ni}_{45}$ ) before increasing significantly to a maximum

value of 180 at  $\text{Ti}_{63}\text{Ni}_{37}$ . With increasing Ti content the luminance drops to a value of around 80 at  $\text{Ti}_{71}\text{Ni}_{29}$ . The luminance then stays almost constant up to a composition of  $\text{Ti}_{90}\text{Ni}_{10}$ .

The Seebeck coefficient for  $\text{Ti}_5\text{Ni}_{95}$  is around  $-5.5 \mu\text{VK}^{-1}$ , increasing rapidly with increasing Ti content and reaching a maximum value of  $4 \mu\text{VK}^{-1}$  for a composition of around 22 at.% Ti. For compositions between  $\text{Ti}_{22}\text{Ni}_{78}$  and around  $\text{Ti}_{50}\text{Ni}_{50}$ , the Seebeck values show some scattering, with a local minimum of  $-3 \mu\text{VK}^{-1}$  at  $\text{Ti}_{24}\text{Ni}_{76}$ . Generally, the values decrease with increasing Ti content. At a composition of  $\text{Ti}_{63}\text{Ni}_{37}$  a local minimum of  $-5.5 \mu\text{VK}^{-1}$  was identified. For further increasing Ti concentration the Seebeck coefficient increases again to  $-2.5 \mu\text{VK}^{-1}$  for around 90 at.% Ti.

On the Ni-rich side of the resistivity plot, an increase of the values was identified, peaking at around  $3.5 \mu\Omega\text{m}$  for a composition close to  $\text{Ti}_{25}\text{Ni}_{75}$ . With further increasing Ti content the resistivity decreases, showing a local minimum of around  $1.2 \mu\Omega\text{m}$  close to a composition of  $\text{Ti}_{44}\text{Ni}_{56}$ . The resistivity increases for higher Ti content again up to a composition of  $\text{Ti}_{64}\text{Ni}_{36}$  where it stays almost constant at a resistivity of  $2.3 \mu\Omega\text{m}$  to  $\text{Ti}_{90}\text{Ni}_{10}$ .

For a composition of around  $\text{Ti}_{63}\text{Ni}_{37}$  a strong correlation between the electrical resistivity, luminance and Seebeck coefficient was identified. All three measured functional properties show a distinct feature for this composition. These features correspond well with the  $\text{Ti}_2\text{Ni}$  phase identified in this area. The same can be stated for the composition of  $\text{Ti}_{24}\text{Ni}_{76}$  where the resistivity peaks while luminance and Seebeck coefficient show a significant drop. In this area the  $\text{Ni}_3\text{Ti}$  phase is pronounced. At  $\text{Ni}_{56}\text{Ti}_{44}$  the electrical resistivity shows a local minimum while the progression of the luminance changes from constant to increasing. Here the monoclinic  $\text{NiTi}$  phase is the most prominent phase. No distinct feature can be identified for the Seebeck coefficient for this composition.

Figure 6c) shows the resistivity, luminance and Seebeck coefficient of the Ni-Si binary axis in the Ti-Ni-Si thin film system. For Ni contents lower than 6 at.% the luminance ranges from 70 to 80. With increasing Ni content, the luminance shows a rapid increase to values as high as 140 for a Ni content of around 13 at.%. Between 13 at.% Ni and 28 at.% Ni the luminance decreases showing a local minimum of around 75 at 28 at.% Ni. It is worth noting that the data is scattering significantly between luminance values of 100 and 140 around 9 at.% Ni and 21 at.% Ni. From 28 at.% Ni the values increase up to a local maximum at around 35 at.% Ni and a luminance value of 105. In the range of 35 at.% Ni to 45 at.% Ni the values show a steady decrease with a sudden drop at 36 at.% Ni. The luminance at 45 at.% Ni is 70 and the values remain fairly constant up to 55 at.% Ni. With higher Ni content the luminance shows a sharp spike with a maximum value of 100 at 57 at.% Ni before falling to 65 at 62 at.% Ni. This luminance value is nearly constant up to 67 at.% Ni. With increasing Ni content, the luminance values increase to around 80 at 77 at.% Ni, showing a distinct spike at 74 at.% Ni for a luminance value of 110. In the compositional range between 77 at.% Ni and 86 at.% Ni the values remain constant on average at a value of 80. Luminance values then increase for Ni concentration above 86 at.% showing a maximum of 130 at 94 at.% Ni. At 96 at.% the luminance shows a distinct dip to a luminance of 85 before rising to 100 for values close to pure Ni ( $\text{Ni}_{98}\text{Si}_2$ ).

The Seebeck coefficients for measurement areas with a Ni content below 5 at.% were excluded from the plot in figure 6 c). With increasing Ni content from 5 at.% Ni, the Seebeck coefficient drops fairly linearly from around  $7.5 \mu\text{VK}^{-1}$  to around  $-2 \mu\text{VK}^{-1}$  for  $\text{Ni}_{15}\text{Si}_{85}$ . Up to a Ni content of 31 at.%, the Seebeck coefficient stays nearly constant at this value. For further increasing Ni content the Seebeck coefficient decreases linearly, reaching a local minimum at 62 at.% Ni ( $-8 \mu\text{VK}^{-1}$ ). In the range from 62 at.% Ni to 68 at.% Ni, the Seebeck coefficient increases linearly to  $-6 \mu\text{VK}^{-1}$  before dropping to a local minimum of  $-12 \mu\text{VK}^{-1}$  at 70 at.% Ni. With further increasing

Ni content the Seebeck coefficient increases again to  $-4 \mu\text{VK}^{-1}$  at  $\text{Ni}_{74}\text{Si}_{25}$ . For Ni content  $> 74$  at.% the Seebeck coefficient decreases, reaching a local minimum at 92 at.% Ni of  $-11 \mu\text{VK}^{-1}$  before increasing slightly to  $-10.5 \mu\text{VK}^{-1}$  for  $\text{Ni}_{98}\text{Si}_2$ .

For Ni contents  $< 12$  at.%, the resistivity is too high to be experimentally accessible with the used measurement technique. With increasing Ni content, the resistivity decreases, reaching a local minimum of  $0.3 \mu\Omega\text{m}$  at around 44 at.% Ni. The resistivity increases with further increased Ni content reaching a local maximum at 55 at.% with a resistivity of  $1.1 \mu\Omega\text{m}$ . Between 55 at.% Ni and 62 at.% Ni the resistivity decreases again to  $0.5 \mu\Omega\text{m}$  with a small spike at 60 at.% Ni and a resistivity value of  $0.75 \mu\Omega\text{m}$ . With further increasing Ni content the resistivity increases, reaching a local maximum at around 74 at.% Ni and  $1.4 \mu\Omega\text{m}$ . For Ni contents  $> 74$  at.% Ni, the resistivity decreases linearly reaching values as low as  $0.2 \mu\Omega\text{m}$  for  $\text{Ni}_{98}\text{Si}_2$ .

A transition from descending to constant values appears in the Seebeck plot at the local maximum in the luminance plot at  $\text{Ni}_{15}\text{Si}_{85}$ . In this compositional area the Si and  $\text{NiSi}_2$  phases coexist.  $\text{Ni}_{15}\text{Si}_{85}$  could mark a transition for Si to  $\text{NiSi}_2$  as the dominant phase in the thin film. It is worth noting that the luminance values in this area show some scattering. No such distinct feature can be identified in the resistivity plot. For a composition of  $\text{Ni}_{44}\text{Si}_{56}$  the resistivity shows a local minimum as well as a transition from descending to fairly constant values in the luminance. The Seebeck coefficient however is decreasing with a constant slope in this area. Here the NiSi phase is dominant, which is a known low resistivity phase in Ni-Si. At  $\text{Ni}_{55}\text{Si}_{45}$  a local maximum of the electrical resistivity can be identified that coincides with a transition from fairly constant luminance values to a sharp increase. However, no such characteristic is found in the Seebeck coefficient plot for this composition. Here the  $\text{Ni}_3\text{Si}_2$  phase is pronounced. For a composition of  $\text{Ni}_{62}\text{Si}_{38}$  both the electrical resistivity and the Seebeck coefficient show a local

minimum while the luminance shows a transition from a descending trend to constant values.

Here the  $\text{Ni}_2\text{Si}$  phase is pronounced. At  $\text{Ni}_{74}\text{Si}_{26}$  both the resistivity and the Seebeck coefficient show a local maximum while the luminance shows a spike. Here the XRD peaks of the  $\text{Ni}_3\text{Si}$  phase show highest intensity.

Regions of comparatively high Seebeck coefficient are shown in table 1. The Seebeck coefficient show a metallic characteristic and are comparatively low compared to other silicides investigated for their thermoelectric performance [36, 46].

**Table 1: Composition, Seebeck coefficient and dominant phase of measurement areas with high Seebeck coefficient in the thin-film system Ti-Ni-Si.**

Composition	Seebeck coefficient in $\mu\text{VK}^{-1}$	Dominant Phase
$\text{Ti}_1\text{Ni}_{91}\text{Si}_8$	-11	Ni
$\text{Ti}_1\text{Ni}_{71}\text{Si}_{28}$	-12	$\text{Ni}_3\text{Si}$
$\text{Ti}_{14}\text{Ni}_{76}\text{Si}_{10}$	8	$\text{TiNi}_3$
$\text{Ti}_{15}\text{Ni}_{45}\text{Si}_{40}$	-11	$\text{TiNi}_4\text{Si}_3$

## Conclusions

A thin-film materials library of the Ti-Ni-Si system has been fabricated and analyzed using high-throughput methods. The established phase diagram is in fair agreement with published works in this system so far.

Functional properties, namely the Seebeck coefficient, electrical resistivity and luminance, have been measured and correlated to each other as well as to structural properties of the material library. In certain cases, the single-phase regions could be easily correlated with extrema in the functional properties as shown for e.g. the Ti<sub>2</sub>Ni phase. As functional properties like the electrical resistivity or luminance can be obtained easily and quickly, they offer the possibility to aid the structural analysis or serve as a quality control mechanism of thin films.

The Seebeck coefficients in the system are low compared to other silicide systems. The highest measured Seebeck coefficient is -12  $\mu\text{VK}^{-1}$  in a measurement area where the Ni<sub>3</sub>Si phase is very pronounced. While this class of materials is very promising, a further improvement is needed to make them competitive for thermoelectric applications.

## Acknowledgements

## References

- 
- <sup>1</sup> Peiqi Xuan, J. Bokor, IEEE Electron Device Lett. 2003, 24, 634.
  - <sup>2</sup> A. Guldan, V. Schiller, A. Steffen, P. Balk, *Thin Solid Films* **1983**, 100, 1.
  - <sup>3</sup> E. G. Colgan, M. Mäenpää, M. Finetti, M.-A. Nicolet, *JEM* **1983**, 12, 413.
  - <sup>4</sup> J. A. Kittl, M. A. Pawlak, C. Torregiani, A. Lauwers, C. Demeurisse, C. Vrancken, P. P. Absil, S. Biesemans, C. Detavernier, J. Jordan-Sweet, C. Lavoie, *Appl. Phys. Lett.* **2007**, 91, 232102.
  - <sup>5</sup> Z. Zhang, P.-E. Hellström, M. Östling, S.-L. Zhang, J. Lu, *Appl. Phys. Lett.* **2006**, 88, 43104.
  - <sup>6</sup> C.-Y. Lee, M.-P. Lu, K.-F. Liao, W.-W. Wu, L.-J. Chen, *Appl. Phys. Lett.* **2008**, 93, 113109.
  - <sup>7</sup> Hyun-Kuk Park, Ik-Hyun Oh, Jun-Ho Jang, Hyun-Taek Shon, Ho-Sung Kim, In-Jin Shon, *Journal of Ceramic Processing Research* **2016**, 17 (3), 191.
  - <sup>8</sup> K. Ohira, Y. Kaneno, T. Takasugi, *Materials Science and Engineering: A* **2005**, 399, 332.
  - <sup>9</sup> C. L. Ma, T. Takasugi, S. Hanada, *Mater. Trans., JIM* **1995**, 36, 30.
  - <sup>10</sup> Z. Du, S. N. Ellis, R. A. Dunlap, M. N. Obrovac, *J. Electrochem. Soc.* **2015**, 163, A13-A18.
  - <sup>11</sup> Z. WEN, S. JI, J. SUN, F. TIAN, R. TIAN, J. XIE, *Rare Metals* **2006**, 25, 77.
  - <sup>12</sup> G. Wang, L. Sun, D. Bradhurst, S. Zhong, S. Dou, H. Liu, *Journal of Alloys and Compounds* **2000**, 306, 249.

- <sup>13</sup> S.-B. Son, S. C. Kim, C. S. Kang, T. A. Yersak, Y.-C. Kim, C.-G. Lee, S.-H. Moon, J. S. Cho, J.-T. Moon, K. H. Oh, S.-H. Lee, *Adv. Energy Mater.* **2012**, 2, 1226.
- <sup>14</sup> C.-M. Chang, Y.-C. Chang, C.-Y. Lee, P.-H. Yeh, W.-F. Lee, L.-J. Chen, *J. Phys. Chem. C* **2009**, 113, 9153.
- <sup>15</sup> Y. Fu, H. Du, W. Huang, S. Zhang, M. Hu, *Sensors and Actuators A: Physical* **2004**, 112, 395.
- <sup>16</sup> J. Mohd Jani, M. Leary, A. Subic, M. A. Gibson, *Materials & Design (1980-2015)* **2014**, 56, 1078.
- <sup>17</sup> C. Naresh, P. S. C. Bose, C. S. P. Rao, *IOP Conf. Ser.: Mater. Sci. Eng.* **2016**, 149, 12054.
- <sup>18</sup> I. Shuro, H. H. Kuo, T. Sasaki, K. Hono, Y. Todaka, M. Umemoto, *Materials Science and Engineering: A* **2012**, 552, 194.
- <sup>19</sup> K. L. Holman, E. Morosan, P. A. Casey, L. Li, N. P. Ong, T. Klimczuk, C. Felser, R. J. Cava, *Crystal Structure and Physical Properties of Mg<sub>6</sub>Cu<sub>16</sub>Si<sub>7</sub>-type M<sub>6</sub>Ni<sub>16</sub>Si<sub>7</sub>, for M = Mg, Sc, Ti, Nb, and Ta*, arXiv:0708.0179.
- <sup>20</sup> X. Zhao, L. Ma, Y. Yao, Y. Ding, X. Shen, *Energy Environ. Sci.* **2010**, 3, 1316.
- <sup>21</sup> Z. WANG, H. WU, N. LIN, X. YAO, Z. HE, X. LIU, *Surf. Rev. Lett.* **2017**, 24, 1750028.
- <sup>22</sup> H. M. Wang, L. X. Cai, *SSP* **2006**, 118, 235.
- <sup>23</sup> B.-C. Lu, Y.-L. Wang, J. Xu, *J. Alloys Compd.* **2009**, 475 (1-2), 157-164.
- <sup>24</sup> Y.-w. Kim, *Intermetallics* **2013**, 38, 4-8.
- <sup>25</sup> K. Ibrahim, N. Elbagoury, Y. Fouad, *Journal of Alloys and Compounds* **2011**, 509, 3913.
- <sup>26</sup> S. F. Hsieh, S. K. Wu, H. C. Lin, *Journal of Alloys and Compounds* **2002**, 339, 162.
- <sup>27</sup> J.-H. Kim, M.-S. Choi, T.-H. Nam, *Met. Mater. Int.* **2001**, 7, 207.
- <sup>28</sup> J. Wang, K. Li, X. Song, L. Guo, W. Li, Z. Li, *Mater. Sci. Eng. A* **2012**, 547, 12-18.
- <sup>29</sup> X.-D. Xiang, I. Takeuchi (Eds.), "Combinatorial Materials Synthesis" **2003**, Marcel Dekker Inc., New York.
- <sup>30</sup> A. Janghorban, J. Pfetzinger-Micklich, J. Frenzel, A. Ludwig, *Adv. Eng. Mater.* **2014**, 16, 588.
- <sup>31</sup> V. Y. Markiv, E. I. Gladyshevskii, P. I. Krypyakevych, T. I. Fedoruk, L. A. Lysenko, Ti-Ni-Si Phase Diagram, ASM Alloy Phase Diagrams Database, P. Villars, editor-in-chief; H. Okamoto and K. Cenual, section editors; <http://www.asminternational.org>, ASM International, Materials Park, OH, 2016.
- <sup>32</sup> V. Y. Markiv, E. I. Gladyshevskii, P. I. Krypyakevych, T. I. Fedoruk, Ti-Ni-Si Phase Diagram, ASM Alloy Phase Diagrams Database, P. Villars, editor-in-chief; H. Okamoto and K. Cenual, section editors; <http://www.asminternational.org>, ASM International, Materials Park, OH, 2016.
- <sup>33</sup> X. Hu, G. Chen, C. Ion, K. Ni, Ti-Ni-Si Phase Diagram, ASM Alloy Phase Diagrams Database, P. Villars, editor-in-chief; H. Okamoto and K. Cenual, section editors; <http://www.asminternational.org>, ASM International, Materials Park, OH, 2016.
- <sup>34</sup> T. Tokunaga, K. Hashima, H. Ohtani, M. Hasebe, *Mater. Trans.* **2004**, 45 (5), 1507-1514.
- <sup>35</sup> F. Weitzer, M. Naka, N. Krendelsberger, F. Stein, C. He, Y. Du, J. C. Schuster, *Z. anorg. allg. Chem.* **2010**, 636, 982.
- <sup>36</sup> A. Nozariasbmarz, A. Agarwal, Z. A. Coutant, M. J. Hall, J. Liu, R. Liu, A. Malhotra, P. Norouzzadeh, M. C. Öztürk, V. P. Ramesh, Y. Sargolzaeiaval, F. Suarez, D. Vashae, *Jpn. J. Appl. Phys.* **2017**, 56, 05DA04.
- <sup>37</sup> M. I. Fedorov, G. N. Isachenko, *Jpn. J. Appl. Phys.* **2015**, 54, 07JA05.
- <sup>38</sup> S. Thienhaus, D. Naujoks, J. Pfetzinger-Micklich, D. König, A. Ludwig, *ACS combinatorial science* **2014**, 16, 686.
- <sup>39</sup> R. Löbel, S. Thienhaus, A. Savan, A. Ludwig, *Mater Sci Eng A* **2008**, 481-482, 151-155.
- [40] S. Thienhaus, S. Hamann, A. Ludwig, *Sci. Technol. Adv. Mater.* **2011**, 12, 054206.
- [41] S. Thienhaus, D. Naujoks, J. Pfetzinger-Micklich, D. König, A. Ludwig, *ACS Comb. Sci.* **2014**, 16, 686.
- [42] P. Ziolkowski, G. Karpinski, T. Dasgupta, E. Müller, *Phys. Status Solidi A* **2013**, 210, 89.

---

<sup>43</sup> P. Ziolkowski, M. Wambach, A. Ludwig, E. Müller, [\*ACS Comb. Sci.\* 2018, 20, 1, 1-18](#)

<sup>44</sup> A. Zhou, W. Wang, X. Yao, B. Yang, J. Li, Q. Zhao, C. Wang, D. Xu, P. Ziolkowski, E. Mueller, *Applied Thermal Engineering*, Volume 107, 2016, Pages 552-559, DOI: <https://doi.org/10.1016/j.applthermaleng.2016.05.037>.

<sup>45</sup> X. Hu, G. Chen, C. Ion, K. Ni, *JPE* **1999**, 20, 508.

<sup>46</sup> M. J. Newton, S. White, C. Estherby, A. Gomez, *PAMR* **2016**, 3, 113.